To cite this article: ZHANG Y Y, WU C S, WANG J C, et al. Direct numerical simulation of flow around a 3D finite square cylinder using the Sunway Taihu Light[J/OL]. Chinese Journal of Ship Research, 2022, 17(3). http://www.ship-research.com/en/article/doi/10.19693/j.issn.1673-3185.02595.

DOI: 10.19693/j.issn.1673-3185. 02595

Direct numerical simulation of flow around a 3D finite square cylinder using the Sunway TaihuLight

*ZHANG Yaying**, *WU Chengsheng*, *WANG Jianchun*, *JIN Yixing*

China Ship Scientific Research Center, Wuxi 214082, China

Abstract: [**Objective**] This paper aims to study the application effects of heterogeneous supercomputing platforms based on domestic processors of China in the field of ship hydrodynamics. [**Methods**] With the Sunway TaihuLight supercomputer, the direct numerical simulation of flow around a three-dimensional (3D) finite square cylinder with Re = 250 is conducted by the programming method of MPI + Athread, the results of which are verified and analyzed. In the simulation, the maximum number of grids is 245.76 million (t = 600 s, dt = 0.001), and the maximum parallel size is 133 120 cores. [**Results**] According to the statistics, the calculation can be completed in a few days under the parallel scale of 133 120 cores using 245.76 million grids. In addition, the simulations reveal that the vortex shedding is synchronous in different cross-sections of a 3D finite square cylinder when the flow around it is in motion. Upon the comparison of the wake flow fields of the flow around the square cylinder of different slenderness ratios, it is found that when the slenderness ratio is 2, the wake vortex structure is a long straight secondary streamwise vortex structure; otherwise, it is an antisymmetric Karman vortex. [**Conclusion**] These results indicate that multilevel parallel computing using the Sunway TaihuLight supercomputer can effectively reduce the time consumption caused by the grid scale increase in small-scale grids, which has broad application prospects in ship hydrodynamics.

Key words: flow around a three-dimensional finite square cylinder; direct numerical simulation; parallel computing; Sunway TaihuLight supercomputer

CLC number: U661.1

0 Introduction

With the development of the shipbuilding industry and ship hydrodynamics, ship design and theoretical investigation require higher accuracy of numerical simulation and more sophisticated geometric models, which results in an exponential increase in the grid size employed for calculation. Furthermore, with the failure of Moore's law, the performance of single-core processors has been limited and is no longer capable of meeting the needs of scientific research and design, and parallel computing has emerged as a crucial technology in the field of computational fluid dynamics (CFD).

Thanks to the rapid expansion of computing hardware, the architecture of supercomputers is shifting from homogeneous to heterogeneous. Compared to homogeneous systems with distributed parallel computing, heterogeneous systems can achieve finer-grained parallelism by utilizing acceleration devices such as the graphics processing unit (GPU), many integrated cores (MIC), and slave-core arrays within a single process, and they remove the constraints of single-chip

frequency on hardware computing capacity to enable supercomputers to achieve significant improvements in computational performance. Meanwhile, finer-grained parallelism will result in several levels

Received: 2021 − 11 − 17 **Accepted**: 2022 − 04 − 03

Supported by: Hydrodynamic Preliminary Research Project in the 14th Five-Year Plan Period (50907070201)

Authors: ZHANG Yaying, male, born in 1994, master degree, assistant engineer

WU Chengsheng, male, born in 1976, PhD, professor

WANG Jianchun, male, born in 1989, master degree, engineer

JIN Yixing, male, born in 1990, master degree, engineer

***Corresponding author**: ZHANG Yaying

of data distribution, which further complicates the communication process, especially in CFD. On the one hand, for incompressible flows, the governing equations are coherently velocity-pressure coupled due to the limited adaptation of equations and algorithms to high-performance computing, and the data correlation caused by implicit and semi-implicit algorithms creates a significant barrier to multi-stage parallelism. On the other hand, due to insufficient memory or instruction processing capacity of the acceleration device in comparison to the CPU, adjustments to the data structure and solution process are required on the basis of the acceleration device, which is a substantial and complicated effort. As a result, the use of heterogeneous supercomputing systems is both an opportunity and a challenge for parallel computing in ship CFD.

In recent years, as the autonomation requirements of the computer-aided engineering (CAE) software for ship hydrodynamics have been raised increasingly in recent years, the combination of domestic software and hardware of China has become the only method to build an independent and controllable CFD system in an all-round way. In this paper, on the basis of Sunway TaihuLight, a heterogeneous supercomputing platform, we use the hybrid programming method of MPI + Athread to parallelize the independent codes, and the semi-implicit method for pressure linked equations (SIMPLE) is employed to numerically simulate the flow around a three-dimensional (3D) finite square cylinder as a case study.

1 Parallel scheme

Sunway TaihuLight is the world's first supercomputer with a peak computing speed of more than one billion times, and it was ranked first among the top 500 computers in the world in terms of performance from 2016 to 2017[1]. The computing system is based on the heterogeneous many-core processor SW26010, which can perform multilevel parallel computing in a heterogeneous manner using master and slave cores and has been used in many fields, including numerical simulation of earth sciences, molecular simulation, and matrix solving [2].

The Sunway TaihuLight supercomputer has an auxiliary computing system and a high-speed computing system. The former uses a processor of ×86 system architecture, while the latter employs the self-developed SW26010 processor of China. As shown in Fig. 1, the SW26010 processor has four core groups, each with one master core and 64 slave cores. The parallelism of the slave cores is controlled by the master core, which uses the accelerated thread library Athread [3] for operations such as the switching of slave cores and data transfer.

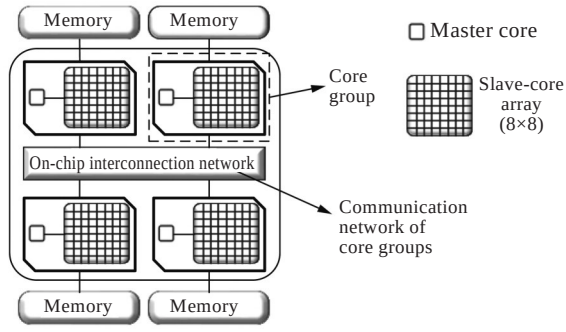

Fig. 1 The structure of SW26010 processor

The SW26010 processor has a unique architecture that enables process-level and thread-level parallel processing across core groups and slave cores, respectively. The process-level parallelism described in this paper employs a grid partitioning approach, in which the grid is segmented according to the number of processes and assigned to different core groups for computation, with data exchange between processes implemented by a message passing interface (MPI). Due to the slave core's limited memory (64 kB) and the fact that communication can only take place in the same row or column, the loop parallelism approach is employed to transport data in batches to the slave core for thread-level computing. Fig. 2 shows the data allocation pattern in parallel computing.

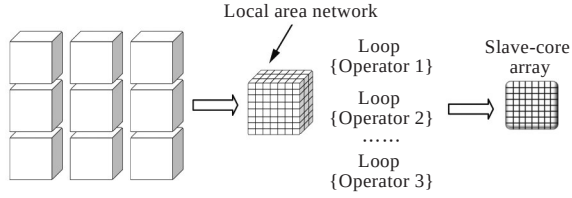

Fig. 2 Data allocation in parallel computing

We examined the parallelism effects of the SIMPLE algorithm and direct numerical simulation approach to validate the feasibility of the above parallel method. With the 3D lid-driven cubic cavity flow as the model and a Reynolds number of Re = 1 000, the parallel acceleration effect under various grid sizes and numbers of processes is investigated.

To demonstrate the characteristics of multi-level parallelism, we displayed such parallelism effects as the speedup and parallel efficiency of single-level MPI parallelism and multi-level MPI + Athread

parallelism. The reference for estimating the speedup was set to be the time consumption of a single master core. Given the functional and memory differences between master and slave cores, the parallel efficiency of MPI was evaluated with a single master core as the reference, and the parallel efficiency of MPI + Athread was assessed with a single core group as the reference. Fig. 3 demonstrates the parallel speedup fluctuation curves of the two parallel modes, MPI and MPI + Athread, under different grid sizes, while Table 1 shows the parallel efficiency.

According to the results in Table 1, the parallel efficiency of MPI is greater than 50% for 128 processes, but the core-group-based scaling efficiency

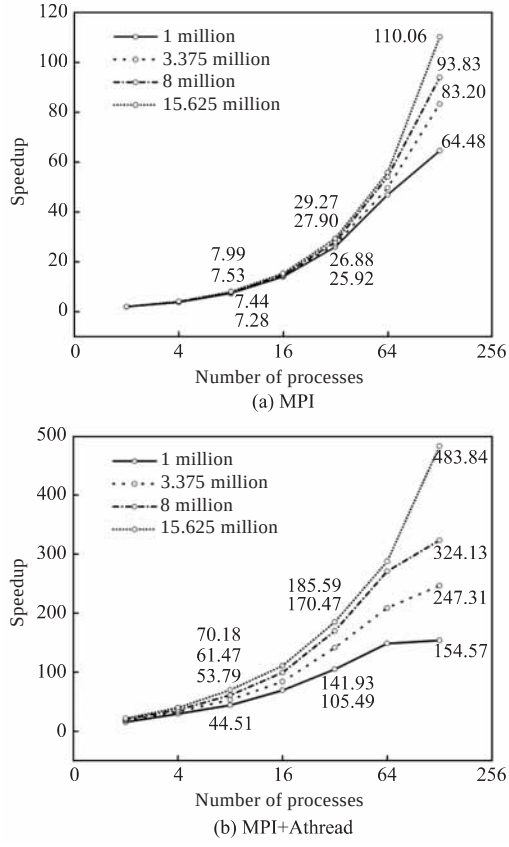

Fig. 3 Speedup curves of direct 3D numerical simulation using SIMPLE algorithm

Table 1 The parallel efficiency of MPI/MPI + Athread for 3D cavity driven flow

Number of grids/million	MPI / MPI+Athread/%			
	4 processes	16 processes	64 processes	128 processes
1 (100×100×100)	93.2/84.88	87.14/53.35	73.07/28.50	50.35/14.78
3.375 (150×150×150)	95.37/87.57	89.68/55.23	77.39/34.30	65.42/20.25
8 (200×200×200)	96.35/90.84	91.24/59.46	84.31/40.48	73.30/24.16
15.625 (250×250×250)	99.94/91.34	95.47/62.95	87.03/40.82	85.98/34.24

Note: The reference for parallel efficiency calculation: MPI (the computation time of a single master core); MPI + Athread (time consumption per core group: master core + slave core group).

of MPI + Athread is poor. In combination with the study of factors influencing the slave-core parallel acceleration of the SW26010 processor in Reference [4], we found that the causes of the above phenomena include the following aspects:

1) The communication process of slave core computing increases overall communication time consumption and decreases parallel efficiency.

2) As the number of processes rises, the workload of an individual process declines. According to Reference [4], this will result in a decrease in the proportion of computing time and an increase in the proportion of communication time, which further leads to a considerable fall in the speedup of slave-core parallel computing.

The speedup curves reveal that when the number of grids is 15.625 million, the 128-process multi-level parallel speedup reaches 483.84x, and the acceleration effect is better as the grid size grows. Thus, it is feasible to adopt the parallel scheme shown in Fig. 2 and use a billion-level grid size for direct numerical simulation of flow around a 3D finite square cylinder on the basis of the SIMPLE algorithm, and fast computing can be accomplished with limited hardware resources.

2 Computational model and governing equations

This research focuses on the flow phenomenon of the flow around a 3D finite square cylinder, which is commonly observed in high-rise buildings, maritime engineering, and traffic engineering. Previous research has concentrated on the flow around a 2D square cylinder. In engineering practice, however, it is typically a finite square cylinder with one end fixed and the other end free, as illustrated in Fig. 4. In the figure, H represents the height of the square cylinder; d represents the width of the cross-section, and u_∞ denotes the incoming flow velocity. Studies show that the slenderness ratio H/d of the square cylinder has a substantial effect on the wake flow. Sakamoto and Arie [5] found that the slenderness ratio of the square cylinder has a crucial value H_c, and when $H/d < H_c$, the entire wake flow region is controlled by the downwash flow separated from the free end, and they predicted that H_c is around 2. Fig. 5 depicts the vortex structure model of the flow around a 3D finite square cylinder at $H/d > H_c$ proposed by Wang et al [6]. The model indicates that the wake flow is an antisymmetric Karman vortex.

The flow medium in this case is an incompress-

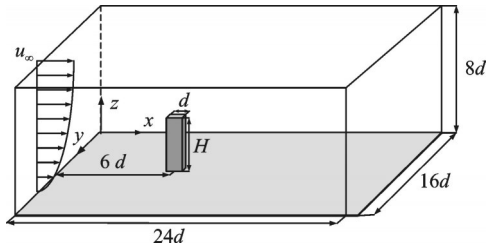

Fig. 4 3D computational model of flow around a finite square cylinder

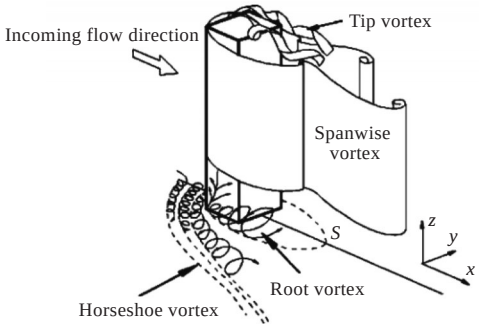

Fig. 5 3D wake vortex structure of flow around a finite square cylinder [6]

ible viscous fluid. According to Fig. 4, the width d is chosen as the characteristic length, and the velocity at infinity is the characteristic velocity. Therefore, the governing equations in the integral form are as follows:

$$\begin{cases} \oint_S \boldsymbol{n}\cdot\boldsymbol{U}\mathrm{d}S=0 \\ \int_V \frac{\partial u}{\partial t}\mathrm{d}V+\oint_S \boldsymbol{n}\cdot\boldsymbol{U}u\mathrm{d}S+\oint_V \frac{\partial P}{\partial x}\mathrm{d}V-\oint_S \upsilon(\boldsymbol{n}\cdot\nabla)u\mathrm{d}S=0 \\ \int_V \frac{\partial v}{\partial t}\mathrm{d}V+\oint_S \boldsymbol{n}\cdot\boldsymbol{U}v\mathrm{d}S+\oint_V \frac{\partial P}{\partial y}\mathrm{d}V-\oint_S \upsilon(\boldsymbol{n}\cdot\nabla)v\mathrm{d}S=0 \\ \int_V \frac{\partial w}{\partial t}\mathrm{d}V+\oint_S \boldsymbol{n}\cdot\boldsymbol{U}w\mathrm{d}S+\oint_V \frac{\partial P}{\partial z}\mathrm{d}V-\oint_S \upsilon(\boldsymbol{n}\cdot\nabla)w\mathrm{d}S=0 \end{cases} \quad (1)$$

where $\boldsymbol{U}$ is the velocity vector; V is the volume of the grid; S is the area of the grid; $\boldsymbol{n}$ is the out-of-plane normal vector; u, v, and w are the velocity components; P is the ratio of pressure to density; t stands for time, and υ is the kinematic viscosity coefficient of the fluid.

The governing equations are discretized by the finite volume method (FVM) with staggered grids. The time term is discretized in the first-order explicit scheme, the advection term in the quadratic upstream interpolation for convective kinetics (QUICK) scheme, and the diffusion term in the central difference scheme, with the details reported in Reference [7]. SIMPLE is used to solve the governing equations.

Operating conditions: Reynolds number $Re = u_\infty d/\upsilon = 250$, the boundary conditions meet the requirement of the velocity inlet on the left side, and the incoming velocity is $u_\infty = 1.0$; the right side is the pressure outlet, $P = 0$; the bottom surface is a solid surface, meeting the non-slip boundary conditions, and all other surfaces satisfy the symmetric boundary conditions.

3 Scaling effect of the grids

The advantage of direct numerical simulation over other approaches is that it can obtain more complete flow field information; nevertheless, the computational domain and grid resolution must fulfill the requirements of the integral scale and dissipative scale, respectively, namely,

$$L > l_0,\ \Delta < \eta,\ l_0/\Delta \sim Re^{3/4},$$

where L is the size of the computational domain; l_0 is the integral scale; Δ is the grid size, and η is the dissipative scale. The integral scale is of the same magnitude as that of the computational domain.

Given that different grid resolutions have varying abilities to capture flow field information, this study employs a three-way encryption strategy and decreases grid size to increase grid resolution. The computation time is calculated to demonstrate the feasibility and superiority of parallel computing in direct numerical simulation. In addition, the flow field differences at the slenderness ratio $H/d = 4$ are compared, and the capability of different grid sizes to capture small-scale flow is reflected in the richness of vortex structure and energy spectrum characteristics.

Table 2 shows the grid resolution, flow field parameters, parallel scale, and computation time under various grid sizes. The SW26010 processor has master and slave cores with a maximum process number of 2 048 and a core number of 133 120. As shown in Table 2, with a time advance of 600 s (6×10^5 iterative time steps), the computation can be completed in one week for the billion-level grid size (245.76 million grids), about 3 days for the 10 million-level grid size (30.72 million grids), and less than a day for the million-level grid size (3.84 million grids). This demonstrates that using the Sunway TaihuLight supercomputer for CFD numerical simulations may expand the grid size by at least one to two orders of magnitude within the restricted scientific research cycle.

The instantaneous vortex structure around the square cylinder and in the wake flow was represented in the following form using the Q criteria[8].

Table 2 Related parameters of numerical simulation for the flow around a square cylinder

Number of grids/million	Grid resolution	Time step/s	*Re*	Number of cores	Number of iteration seps/s	Computation time/h
3.84 (240×160×100)	0.1*d*			33 280		17
30.72 (480×320×200)	0.05*d*	0.001	250	33 280	6×10^5	79
245.76 (960×640×300)	0.025*d*			133 120		160

$$Q=\frac{1}{2}[\|\boldsymbol{S}^2\|-\|\boldsymbol{\Omega}^2\|],\ \boldsymbol{S}_{i,j}=\frac{1}{2}\left(\frac{\partial \boldsymbol{u}_i}{\partial x_j}-\frac{\partial \boldsymbol{u}_j}{\partial x_i}\right),$$
$$\boldsymbol{\Omega}_{i,j}=\frac{1}{2}\left(\frac{\partial \boldsymbol{u}_i}{\partial x_j}+\frac{\partial \boldsymbol{u}_j}{\partial x_i}\right) \quad (2)$$

where $\boldsymbol{u}_j$ is the velocity tensor, and $\boldsymbol{S}_{i,j}$ is the antisymmetric tensor of the velocity gradient; $\boldsymbol{\Omega}_{i,j}$ is the symmetric tensor of the velocity gradient, and the presence of vortices can be assumed when $Q > 0$.

Fig. 6 illustrates the instantaneous vortex structure (Q = 0.01) of the flow field at t = 450 s. The figure shows the horseshoe vortex in front of the square cylinder, the formation of the envelope surface behind the square cylinder, and the antisymmetric vortex in the wake flow, which is compatible with the features of the vortex structure depicted in Fig. 5. The comparison of the computation results at different grid sizes clearly indicates that the vortex structure becomes clearer and more specific as the grid resolution increases. This means that the high-resolution grid is able to capture more flow details.

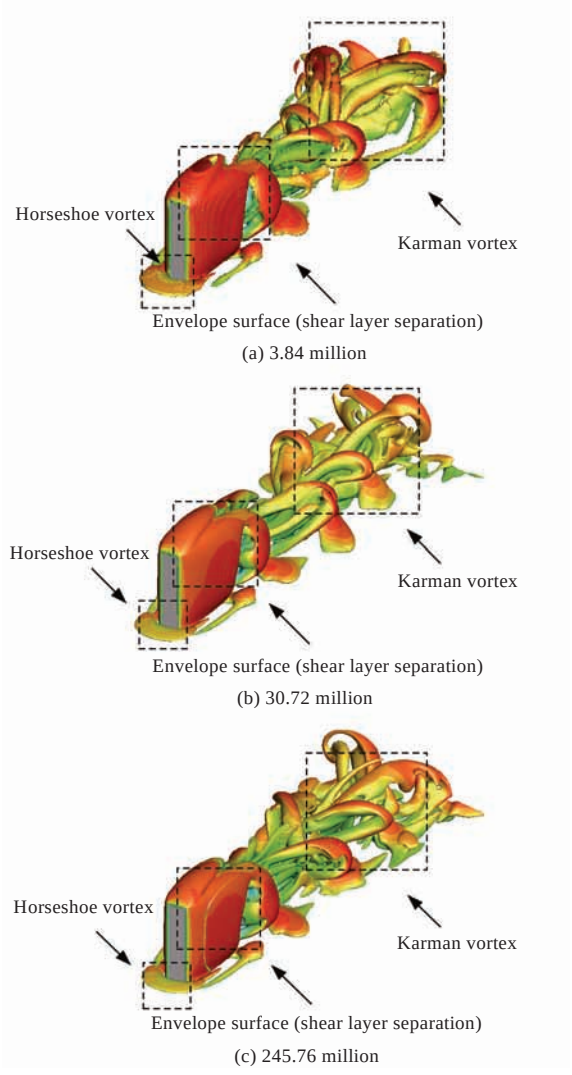

Fig. 6 Instantaneous vortex structures at t = 450 s when Q = 0.01

Two measuring points (x = 15d and x = 22d) just behind the square cylinder (z = 2d, y = 8d) were selected, and Fig. 7 shows the time-history variation curves of their transverse velocity and energy spectrum analysis. The time history variation curves show that the velocity amplitude obtained under the three grid sizes at the same geographical position is approximate. In the energy spectrum analysis curves, it is clearly observed that the characteristic frequencies of the flow field are similar for the three grid sizes. Table 3 lists the basic frequencies and their corresponding amplitude, and it shows that the characteristic frequencies of the flow field calculated in different grid sizes are almost identi-

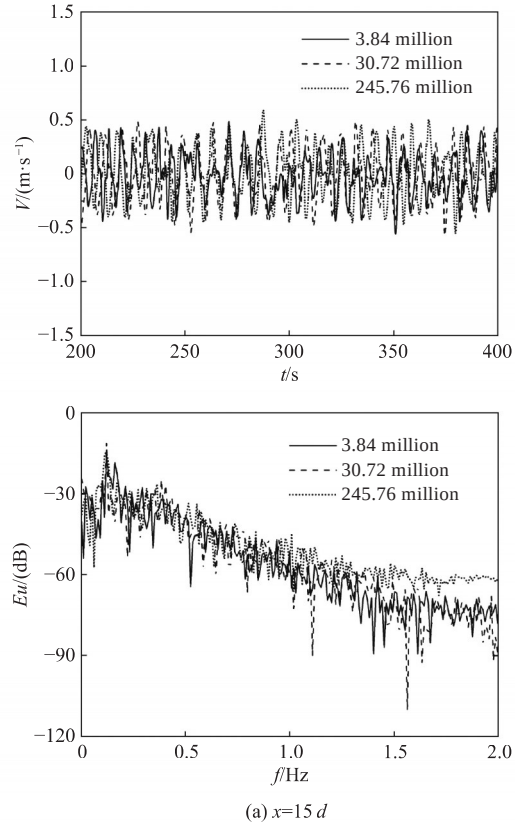

(a) x=15 d

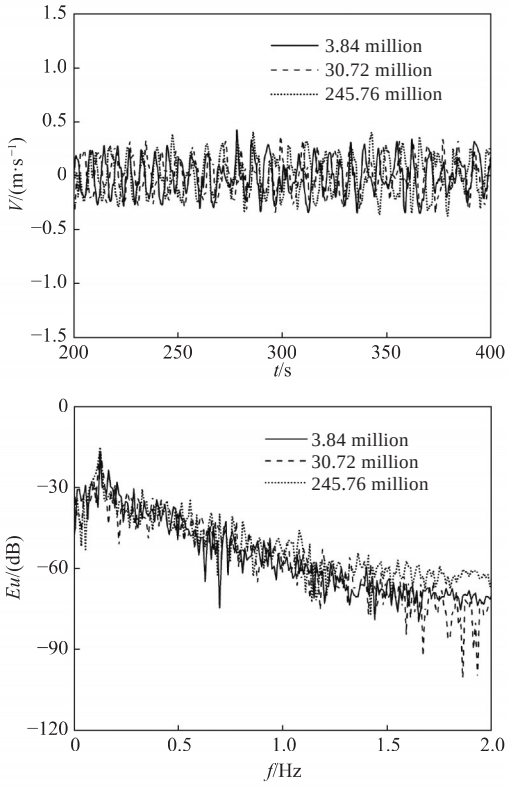

(b) x=22 d

Fig. 7 Time-history variation curves and energy spectrum analysis of transverse velocity under different grid sizes (the position of the measuring point: z = 2d, y = 8d)

Table 3 Characteristic frequencies of flow field under different grid sizes for flow around a square cylinder

Number of grids/million	x=15d		x=22d	
	Basic frequency /Hz	Basic frequency amplitude/dB	Basic frequency /Hz	Basic frequency amplitude/dB
3.84	0.129	−15.96	0.129	−16.46
30.72	0.130	−14.08	0.130	−15.70
245.76	0.130	−13.86	0.130	−14.93

cal, but the energy amplitude in the high-frequency region gradually increases as the grid size increases. This means that the simulation can capture more small-scale motions at higher grid resolutions.

4 Flow characteristic analysis

When the aforementioned computational results are compared under different grid sizes, it is clear that a greater grid resolution is more useful for the capture of the flow phenomena. Considering the computation time and hardware costs, this study used a grid size of 30.72 million to investigate the flow phenomena of flow around a square cylinder. The computational domain size and grid size satisfy the requirements of direct numerical simulation.

To investigate the influence of free-end shear flow on the wake vortex structure, this study will evaluate the field of the flow around a square cylinder with a slenderness ratio of H/d = 4 and compare the differences in the wake vortex structure of the flow around a square cylinder with a slenderness ratio of H/d = 2, 3, and 4.

4.1 Wake vortex characteristics

Fig. 8 displays a contour plot of the instantaneous vorticity ($\boldsymbol{\Omega}_z$) in the z-direction of the flow around a square cylinder. The presence of vortex contours on three cross-sections in the region behind the square cylinder is clearly seen in Fig. 8(a). The comparison of the contours in Fig. 8(b) demonstrates that the contour vortex shedding (hereinafter referred to as vortex shedding) on the three cross-sections is nearly identical. It is also consistent with the findings computed in this study in combination with the vortex shedding model [6] for different cross-sections of the square cylinder illustrated in Fig. 8(c).

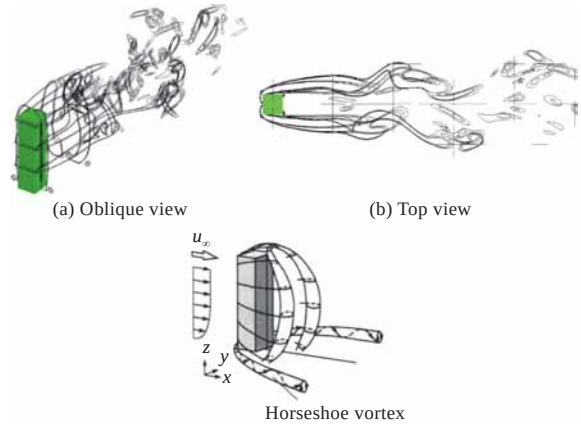

(a) Oblique view (b) Top view

(c) Vortex shedding model of different cross-sections[6]

Fig. 8 Characteristics of vortex distributions on square cylinder cross-section

To further quantify and compare the characteristics of the vortex shedding on different cross-sections, we chose the grid size of 30.72 million for a case study. For horizontal cross-sections of different height (z = 0.5d, 2.0d, and 3.5d), the transverse velocity (in the y direction) of two positions (x = 15d and x = 22d) right behind the square cylinder were detected, and the energy spectrum analysis was performed. The time-history variation curves of transverse velocity in Fig. 9 show that the transverse velocity on different cross-sections has roughly the same phase, either in the near-field region (x = 15d) or in the far-field region (x = 22d). This is consistent with the result shown in Fig. 8(a) regarding the synchronous vortex shedding of each cross-section

of the square cylinder and also agrees with the results given by resistance calculations in Ref. [9].

The comparison of the transverse velocity amplitude indicates that the transverse velocity amplitude on the cross-sections at the bottom or near the free end reduces significantly in contrast with that on the middle cross-section. This means that the solid wall surface of the free end and the bottom has a considerable inhibitory effect on vortex shedding. Furthermore, the comparison of the transverse velocity amplitude at these two sites shows that the amplitude at the far field is lowered to some extent, which indicates that the viscous force is dissipative. The results of the energy spectrum analysis shown in Fig. 9 reveal that the transverse velocity on cross-sections of different heights has the same characteristic frequency, and the energy of the transverse velocity on the middle cross-section is higher, which corresponds to the time-history variation characteristics of transverse velocity.

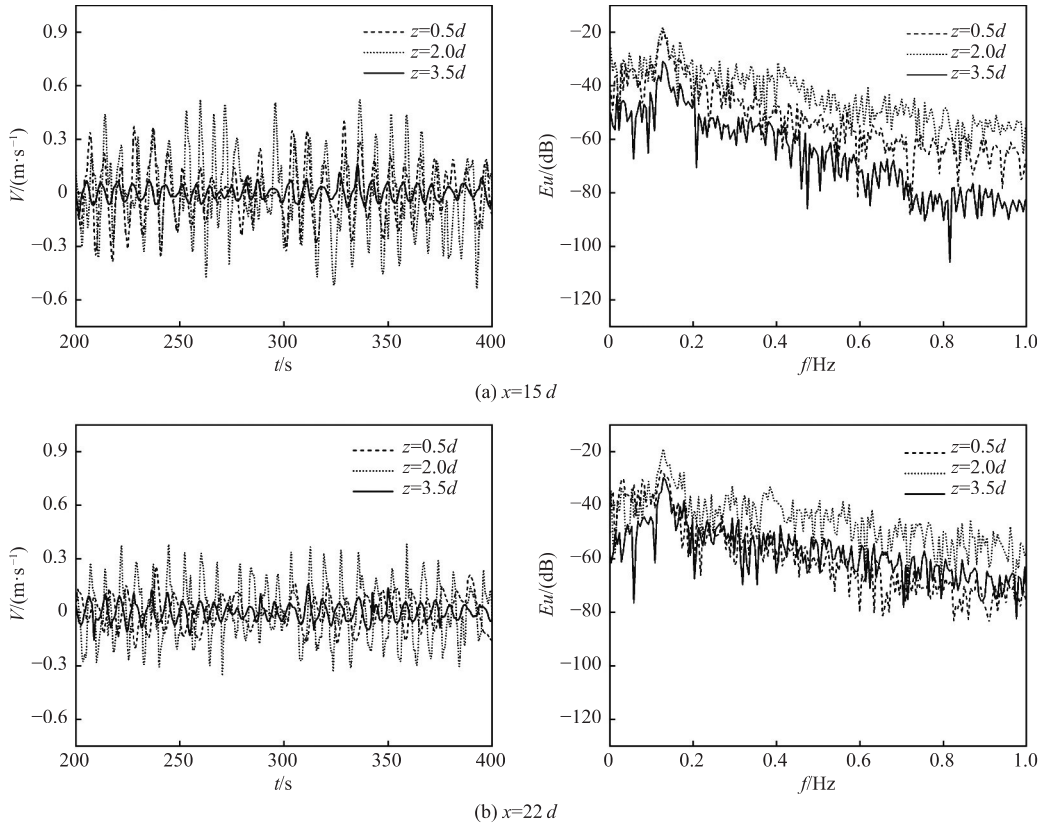

Fig. 9 Time-history variation curves and energy spectrum analysis of transverse velocity on horizontal cross-sections at different heights (the position of the measuring point: $z = 2d$, $y = 8d$)

4.2 Influence of slenderness ratio

Fig. 10 depicts the instantaneous (Q = 0.01) vortex structure for the slenderness ratio of H/d = 2, 3, and 4. As can be seen in the figure, the wake flow retains an antisymmetric Karman vortex at H/d = 3; at H/d = 2, the antisymmetric vortex shedding in the wake flow vanishes completely and emerges as a secondary streamwise vortex structure [10].

The time-history variation curves of transverse velocity at the cross-sectional height of z/H = 0.5 for the square cylinder with different slenderness ratios and the corresponding energy spectrum analysis results are shown in Fig. 11 to clearly demonstrate the characteristics of the flow field around the square cylinder with different slenderness ratios. The transverse velocity amplitude steadily decreases as the slenderness ratio of the square cylinder decreases. The time-history transverse velocity curve changes in a straight line under the slenderness ratio of H/d = 2. The energy spectrum analysis clearly demonstrates that when the slenderness ratio drops, the alternating vortex shedding of the whole flow field steadily reduces, and at H/d = 2, the aforementioned vortex shedding nearly disappears. Table 4 lists the estimated average drag coefficient (C_d) and Strohal number (St) for the flow around the square cylinder with different slenderness ratios. The calculation results of this study are close to the results given by local grid refinement in Reference [10], which indicates that the calculations in this study are valid.

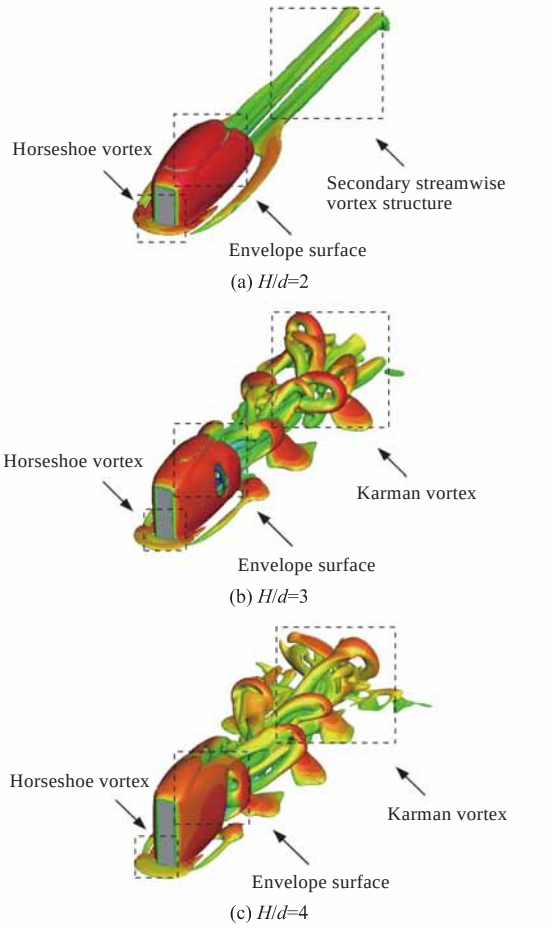

Fig. 10 Instantaneous vortex structures of flow around a 3D finite square cylinder with different slenderness ratios (Q = 0.01)

As the incoming flow velocity is constant, the time average method was adopted for the statistics of turbulent flow, which could more intuitively describe the features of the flow around a square cylinder with different slenderness ratios. Fig. 12 shows the streamline distribution on the longitudinal section (y = 8d) of the flow around a square cylinder with different slenderness ratios. As shown in the figure, there are both upper and lower backflow zones behind the square cylinder in the case of a slenderness ratio of H/d = 3, 4, with the upper backflow zone generated by the downwash flow separated by the shear layer at the free end. The flow direction of the lower (root) backflow zone is opposite to that of the upper backflow zone, and the streamline separation point (saddle point) "+" was formed in the downstream of the flow field in both cases as a result of the opposite direction of vortex shedding on the cross-sections of the upper and lower backflow zones. In contrast, when the slenderness ratio decreased from 4 to 3, the area of the upper backflow zone shrank dramatically, which suggests that

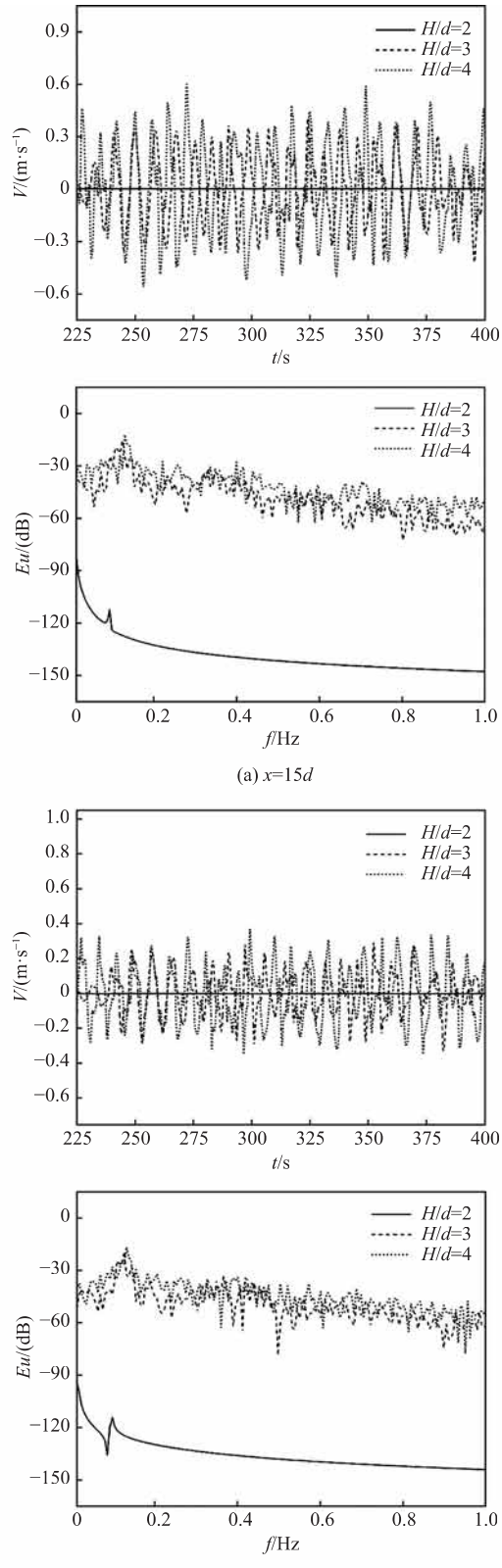

Fig. 11 Time-history variation curves and energy spectrum analysis of transverse velocity of flow around a 3D square cylinder with different slenderness ratios at the cross-sectional height of z/H = 0.5

the intensity of the downwash flow separated by the shear layer at the free end has been significantly weakened. Unlike the flow around the square cylinder with slenderness ratios of 3 and 4, when the

Table 4 Average drag coefficient and Strouhal number of the flow around a 3D finite square cylinder with different slenderness ratios

Case	*H*/*d*	*St*	C_d
Our study	2	0.095	1.075
	3	0.115	1.18
	4	0.130	1.245
Reference[10]	2	0.097	1.08
	3	0.114	1.16
	4	0.124	1.23

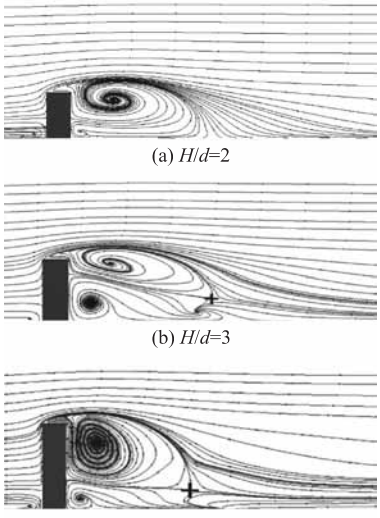

(a) *H*/*d*=2

(b) *H*/*d*=3

(c) *H*/*d*=4

Fig. 12 Streamline distribution of longitudinal section ($y = 8d$) in time average flow field around a square cylinder with different slenderness ratios

slenderness ratio was continuously reduced to 2, no obvious saddle point appeared in the wake flow, and the wake flow was controlled by the downwash flow separated by the shear layer at the free end. The flow field characteristics and the critical slenderness ratio are consistent with the findings described in Reference [5].

5 Conclusions

In this study, the direct numerical simulation of the flow around a 3D finite square cylinder with Re = 250 was performed by the supercomputer Sunway TaihuLight with a grid size of 3.84−245.76 million. Upon the numerical simulation of the flow around a square cylinder with a slenderness ratio of H/d = 4, the grid scaling effect and its corresponding flow field characteristics were summarized and concluded. On this basis, numerical simulation and comparative analysis in the case of H/d = 2, 3 were conducted, and the following findings are obtained.

1) Multi-level parallel computing on Sunway TaihuLight may dramatically improve computational efficiency and the capabilities of large-scale parallel computing.

2) A comparison of the simulation results of different grid sizes reveals that the high-resolution grid helps to capture more information from the flow field. The vortex shedding on cross-sections of different heights is synchronized for flow around a 3D finite square cylinder. The findings of transverse velocity amplitude and energy spectrum analysis of the cross-sections of different heights reveal that both the downwash flow separated by the shear layer at the free end and the viscous force at the bottom surface restrict vortex shedding on adjacent cross-sections.

3) The comparison of the flow around a square cylinder with different slenderness ratios shows that when the slenderness ratio is 2, the downwash flow separated by the shear layer at the free end covers the zone near the rear wall surface of the square cylinder, which suppresses the vortex shedding of the entire square cylinder and leads to the disappearance of the antisymmetric vortex shedding in the wake flow.

In conclusion, multi-level parallel computing based on the supercomputer Sunway TaihuLight has good potential for applications in ship hydrodynamics, but the grid and geometric model used in practical engineering research is more complex than those in this study. Thus, in-depth research is required before its application to the actual engineering fields.

References

[1] ZHANG Y Q, YUAN L, YUAN G X, et al. State-oftheart analysis and perspectives of China HPC development in 2020 [J]. Frontiers of Data & Computing, 2020, 2 (6): 1−10 (in Chinese).

[2] LI Y. Dense matrix eigenvalue solving algorithm and performance optimization based on Sunway Taihulight [D]. Beijing: University of Chinese Academy of Sciences, 2018 (in Chinese).

[3] LI F, LI Z H, XU J X, et al. Research on adaptation of CFD software based on many-core architecture of 100Pdomestic supercomputing system [J]. Computer Science, 2020, 47 (1): 24−30 (in Chinese).

[4] ZHANG Y Y, WU C S, WANG J C, et al. Multi-core processor oriented parallel computation for CFD in hydrodynamics [J]. Ship & Boat, 2021, 32 (4): 15−23 (in Chinese).

[5] SAKAMOTO H, ARIE M. Vortex shedding from a rectangular prism and a circular cylinder placed verti-

cally in a turbulent boundary layer [J]. Journal of Fluid Mechanics, 1983, 126: 147−165.

[6] WANG H F, ZHOU Y. The finite-length square cylinder near wake [J]. Journal of Fluid Mechanics, 2009, 638: 453−490.

[7] TAO W Q. Numerical Heat Transfer [M]. 2nd ed. Xi'an: Xi'an Jiaotong University Press, 2001 (in Chinese).

[8] HUNT J C R, WRAY A A, MOIN P. Eddies, streams, and convergence zones in turbulent flows: N89-24555 [R]. Stanford: Center for Turbulence Research, 1988: 193−208.

[9] GAO J T. Numerical study on free end effect of flow around a cylinder [D]. Harbin: Harbin Engineering University, 2019 (in Chinese).

[10] SAHA A K. Unsteady flow past a finite square cylinder mounted on a wall at low Reynolds number [J]. Computers & Fluids, 2013, 88: 599−615.

基于“神威·太湖之光”的三维有限长方柱绕流直接数值模拟

张亚英*, 吴乘胜, 王建春, 金奕星

中国船舶科学研究中心,江苏 无锡 214082

摘　要:［**目的**］旨在探索基于国产处理器的异构超算平台在船舶水动力学领域的应用效果。［**方法**］基于“神威·太湖之光”超级计算机,采用MPI+Athread的编程方法,对雷诺数*Re*=250的三维有限长方柱绕流进行直接数值模拟,并对模拟结果进行验证与分析。模拟使用的网格规模最大达到245.76百万(*t*=600 s, d*t*=0.001),并行规模最高达到133 120核。［**结果**］经统计,在133 120核并行规模下245.76百万网格规模计算能够在数天之内完成。模拟结果显示,在三维有限长方柱绕流流动中,方柱各横截面具有同步涡脱的特征;对比不同长径比方柱绕流尾流场,发现长径比为2时的尾流涡系结构呈现出长直状的流向涡二次结构,而大于2时则为反对称卡门涡。［**结论**］模拟表明,基于“神威·太湖之光”超级计算机的多级并行计算可有效减少小尺度网格下因规模提升所导致的时间成本,在船舶水动力学领域有较好的应用潜力。

关键词: 三维有限长方柱绕流; 直接数值模拟; 并行计算; “神威·太湖之光”超级计算机